

Cite this: *Environ. Sci.: Nano*, 2025, 12, 1305

## Facet-dependent hematite reactivity in Cr(vi) removal with Fe(II)<sup>†</sup>

Shengnan Zhang, Lingyi Li, Junxue Li and Wei Cheng \*

Hematite displays diverse crystal structures and often coexists with Fe(II), both of which are crucial in controlling the fate and mobility of Cr(vi). However, the mechanisms underlying Cr(vi) removal in the presence of Fe(II) on various hematite facets remain elusive. This study aims to elucidate the facet-dependent reactivity of hematite nanocrystals in conjunction with Fe(II) for the removal of Cr(vi) from aqueous solutions. Hematite nanoplates (HNPs), predominantly composed of {001} facets, and nanorods (HNRs), exposing both {001} and {110} facets, were synthesized and characterized. Their Cr(vi) removal capabilities were evaluated in hematite–Cr(vi) and hematite–Fe(II)–Cr(vi) systems, as well as the Fe(II)–Cr(vi) system. The adsorption of Fe(II) and Cr(vi) on hematite surfaces was highly dependent on the crystal facets and pH, with HNRs demonstrating superior Cr(vi) adsorption over HNPs, especially under acidic conditions. Neutral pH favored Fe(II)–Cr(vi) redox reactions and Fe(II) adsorption. The hematite–Fe(II) couple displayed a synergistic effect in removing Cr(vi) under acidic conditions, which was not observed under neutral conditions. The presence of Fe(II) notably enhanced Cr(vi) adsorption onto hematite, and bound Fe(II) facilitated electron transfer, accelerating Cr(vi) reduction. HNRs–Fe(II) exhibited higher Cr(vi) removal efficiency than HNPs–Fe(II) due to their lower free corrosion potential and improved electron transport properties. This research underscores the potential of facet engineering in optimizing hematite nanocrystals for environmental remediation, specifically in Cr(vi)-contaminated environments.

Received 12th August 2024,  
Accepted 20th November 2024

DOI: 10.1039/d4en00733f

rsc.li/es-nano

### Environmental significance

This study investigates the facet-dependent reactivity of hematite nanocrystals in conjunction with Fe(II) for the removal of Cr(vi). The adsorption of Fe(II) and Cr(vi) on hematite surfaces was shown to be highly dependent on the crystal facets and pH. The hematite–Fe(II) couple displayed a synergistic effect in removing Cr(vi) under acidic conditions. The presence of Fe(II) notably enhanced Cr(vi) adsorption onto hematite, and HNRs–Fe(II) exhibited higher efficiency in Cr(vi) removal. These findings underscore the importance of facet engineering in optimizing hematite nanocrystals for environmental remediation applications, especially in environments contaminated with Cr(vi).

## 1. Introduction

Chromium (Cr), a naturally occurring heavy metal, is highly toxic and exists predominantly in two oxidation states: Cr(III) and Cr(VI). Cr(III) is less toxic due to its general insolubility and immobility under ambient conditions. In contrast, Cr(VI) is highly soluble and mobile in soil and water, posing significant health risks due to its carcinogenic and mutagenic properties.<sup>1</sup> However, its extensive application in industrial processes such as leather tanning, electroplating, metal

finishing, cement production, and textile manufacturing cause significant Cr(VI) emissions into soils.<sup>2,3</sup>

Hematite, a thermodynamically stable iron oxide widely present in soils and sediments, plays a crucial role in controlling the mobility and bioavailability of Cr(VI) in subsurface environments.<sup>4,5</sup> Hematite particles in nature exhibit different crystal structures with various exposed crystal facets, such as {001}, {101}, {110}, {012}, {104}, and {113} *etc.*,<sup>6–9</sup> each characterized by unique reactivity due to different atomic arrangements and electronic configurations.<sup>10–12</sup> These exposed crystalline facets are crucial in processes like adsorption,<sup>4,13,14</sup> catalysis,<sup>15,16</sup> and interfacial electron transfer.<sup>17,18</sup> For example, Huang *et al.*<sup>4</sup> revealed that Cr(VI) species tend to adsorb on {001} and {110} facets in distinct configurations, influencing the Cr(VI) adsorption performance on hematite facets.

Key Laboratory of Catalysis and Materials Science of the State Ethnic Affairs Commission & Ministry of Education, Hubei Province, College of Resource and Environmental Science, South-Central Minzu University, Wuhan 430074, PR China.  
E-mail: wei.cheng@scuec.edu.cn

<sup>†</sup> Electronic supplementary information (ESI) available. See DOI: <https://doi.org/10.1039/d4en00733f>

In anoxic subsurface soil environments, hematite and aqueous Fe(II) often coexist in processes like weathering of Fe(II)-bearing rocks, upwelling of anoxic spring water, acid mine drainage, and microbial iron reduction.<sup>18,19</sup> The complex geochemical interactions involved reactions such as reductive dissolution of hematite, binding of Fe(II) to hematite, and Fe(II)-catalyzed recrystallization of hematite. These processes also relied on exposed facets of hematite. For example, hematite nanocubes exposed with {012} facets have been observed to display higher aqueous Fe(II) adsorption capacity and undergo more intensive Fe atom exchange compared to hematite nanoplates exposed with {001} facets.<sup>18</sup> The distinct affinity of Fe(II) ions for particular hematite facets is inherently linked to the different coordination geometries of Fe(II) at these facets. Huang *et al.*<sup>20</sup> demonstrated that the polar {110} facets are capable of accommodating a higher density of Fe(II) through a five-coordinate binding arrangement compared to the nonpolar {001} facets, which facilitate a six-coordinate binding mode for Fe(II). The coordination of Fe(II) on different facets influences the overall adsorption capacities, catalytic activities and redox behavior of hematite nanocrystals. These properties are vital for the iron cycle and play a critical role in the transformation and transport of environmental pollutants.<sup>5,17,18,21</sup> For example, Huang *et al.*<sup>21</sup> reported that the hematite with {110} facets could confine aqueous Fe(II) of higher density and thus promote the H<sub>2</sub>O<sub>2</sub> decomposition to produce ·OH for more efficient organic contaminants degradation than hematite with nonpolar {001} facets. In contrast, Hao *et al.*<sup>17</sup> demonstrated the facet-dependent reduction activity of hematite–Fe(II) couple by nitrobenzene reduction experiments, with the {001} facets demonstrating higher efficiency in nitrobenzene reduction compared to the {110} facets. Previous studies of the Fe(II)–hematite system have primarily focused on the degradation of organic pollutants. However, this system also holds potential for heavy metal remediation. Specifically, Fang *et al.*<sup>22</sup> showed that surface-bound Fe(II) on hematite can activate oxygen, generating reactive oxygen species that are essential for As(III) oxidation. Jiang *et al.*<sup>5</sup> observed that Fe(II) promotes the adsorption, reduction, and immobilization of Cr(VI) on hematite. Although the facet-dependent adsorption of Cr(VI) and Fe(II) on hematite has been well-documented,<sup>4,18,21</sup> the mechanisms underlying Cr(VI) removal by hematite with various exposed facets in the presence of Fe(II) remain unclear.

The mechanisms of Cr(VI) removal within the hematite–Fe(II)–Cr(VI) system are indeed intricate. Both Fe(II) and Cr(VI) exhibit facet-dependent adsorption onto hematite, and Fe(II) is capable of reducing Cr(VI) to the less toxic Cr(III) through electron transfer.<sup>23–26</sup> Additionally, the reducing property of Fe(II) is typically enhanced upon adsorption onto mineral surfaces compared to the dissolved Fe(II),<sup>27,28</sup> leading to increased Cr(VI) reduction reactivity on hematite. Considering the variety of exposed facets on hematite and its natural co-occurrence with Fe(II), gaining insights into the interfacial

reactions involved in Cr(VI) removal on hematite's different facets in the presence of Fe(II) is crucial for advancing our comprehension of these complex environmental processes.

This study investigates the influence of crystal facets on the Fe(II) redox chemistry in Cr(VI) removal on hematite surfaces, with a focus on the {001} and {110} crystallographic surfaces, which are commonly found in natural settings. The research examines the kinetics of Cr(VI) removal by hematite {001} and {110} crystallites coupled with Fe(II) under both acidic (pH 3 and pH 5) and neutral (pH 7) conditions, aiming to elucidate the crystal facet-dependent mechanism of Cr(VI) removal facilitated by hematite-coupled Fe(II).

## 2. Materials and methods

### 2.1. Chemicals and materials

All chemicals used in this study were of analytical grade or higher, and were utilized without additional processing or purification. 1,2-Propanediamine (C<sub>3</sub>H<sub>10</sub>N<sub>2</sub>) was sourced from Aladdin Industrial Corporation (Beijing, China). Diphenyl carbonyl dihydrazide (C<sub>13</sub>H<sub>14</sub>N<sub>4</sub>O), 1,10-phenanthroline (C<sub>12</sub>H<sub>8</sub>N<sub>2</sub>·H<sub>2</sub>O), and glacial acetic acid (C<sub>2</sub>H<sub>4</sub>O<sub>2</sub>) were procured from Macklin (Shanghai, China). Piperazine-1,4-diethanesulfonic acid (C<sub>8</sub>H<sub>18</sub>N<sub>2</sub>O<sub>6</sub>S<sub>2</sub>, PIPES) was purchased from Merger (Shanghai, China). Potassium chromate (K<sub>2</sub>Cr<sub>2</sub>O<sub>7</sub>), hydrochloric acid (HCl), acetone (C<sub>3</sub>H<sub>6</sub>O), ethanol (C<sub>2</sub>H<sub>5</sub>OH), sodium acetate (CH<sub>3</sub>COONa), ferrous chloride tetrahydrate (FeCl<sub>2</sub>·4H<sub>2</sub>O), ferric chloride hexahydrate (FeCl<sub>3</sub>·6H<sub>2</sub>O), sodium hydroxide (NaOH), sodium chloride (NaCl), and hydroxylamine hydrochloride (HONH<sub>2</sub>·HCl) were all obtained from Sinopharm Group (Shanghai, China).

Ultrapure “Milli-Q” water (specific resistivity, 18.2 MΩ cm<sup>-1</sup>) was used for the preparation of all solutions. A Cr(VI) stock solution with a concentration of 20 mM was prepared by dissolving 58.84 mg of K<sub>2</sub>CrO<sub>4</sub> solid in 200 mL of ultrapure water. In a N<sub>2</sub>-glovebox (MIKROUNA, SUPER) (pO<sub>2</sub> < 1 ppm), 198.81 mg of FeCl<sub>2</sub>·4H<sub>2</sub>O was dissolved in 100 mL of oxygen-free HCl solution (0.1 M) to prepare a Fe(II) stock solution at a concentration of 10 mM, which was then diluted to the desired concentration with oxygen-free water for each experiment. All solutions were purged with N<sub>2</sub> for 4 h before being transferred into the glove box.

### 2.2. Synthesis and characterization of hematite nanocrystals

Two types of hematite nanocrystals with distinct exposed crystal faces were synthesized employing a hydrothermal method as reported in the literature.<sup>15,29</sup> For the synthesis of hematite nanoparticles (HNPs), 3.82 g of FeCl<sub>3</sub>·6H<sub>2</sub>O and 11.2 g of CH<sub>3</sub>COONa were dissolved in 140 mL of ethanol with 9.8 mL of ultrapure water. The solution was then transferred into a Teflon-lined stainless steel autoclave with a capacity of 200 mL and subjected to hydrothermal treatment at 180 °C for 12 h. Finally, the precipitate was collected through centrifugation, washed thoroughly with ethanol and ultrapure water, and subsequently dried at 60 °C in an oven. In the case of hematite nanorods (HNRs), the synthesis

involved dissolving 10.13 g of  $\text{FeCl}_3 \cdot 6\text{H}_2\text{O}$  in 75 mL of ultrapure water, followed by the addition of 75 mL of 1,2-propanediamine. This solution was then heated in a 200 mL Teflon-lined stainless steel autoclave at 180 °C for 12 hours. The resultant precipitates were collected, washed and dried, and further subjected to calcination under an air atmosphere at 400 °C for 2 hours to obtain the HNRs.

The crystal structure of the samples was identified using powder X-ray diffraction (XRD) (D8 Advance, Germany). The analysis was performed using  $\text{Cu K}\alpha$  radiation with a wavelength of 0.15418 nm, scanning over a  $2\theta$  range of 20–80° at a rate of 5°  $\text{min}^{-1}$ . The size and morphology of the synthesized hematite were examined using a FEI Tecnai F20 high resolution transmission electron microscopy (HRTEM, USA) operated at 200 kV. This equipment also enabled the acquisition of lattice fringes and selected-area electron diffraction patterns for the samples, yielding high-resolution images with superior contrast. The  $\text{N}_2(\text{g})$  adsorption/desorption isotherms were recorded at 77 K using a nitrogen adsorption apparatus (JWGB SCI.& TECH, JW-BK132F, China) after the samples had been degassed overnight at 353 K. The Brunauer–Emmett–Teller (B.E.T.) method was applied to calculate the specific surface areas of the hematite nanocrystals. The zeta potential of hematite was measured using a NanoBrook 90Plus zeta analyzer (Brookhaven, USA). Hematite suspensions at a concentration of 0.5  $\text{g L}^{-1}$  were adjusted to a pH range of 4–10 in a 10 mM NaCl solution and allowed to equilibrate for 24 hours under a nitrogen atmosphere. For the zeta potential determination, aliquots were taken, and each sample was analyzed in triplicate, with each analysis consisting of 12 to 30 runs. The final zeta potential values were calculated as the mean of these three measurements. Tafel polarization diagrams were recorded on an electrochemical workstation (CHI-600C, Shanghai Chenghua, China) within a potential range of –0.5 V to 0.5 V at a scan rate of 10  $\text{mV s}^{-1}$  to measure the free corrosion potentials of HNPs and HNRs in the presence of 20  $\mu\text{M}$   $\text{Fe}(\text{II})$  and  $\text{Cr}(\text{VI})$ , as detailed in Text S1†. X-ray photoelectron spectroscopy (XPS) was carried out on an X-ray photoelectron spectrometer (MULT-LAB2000, UK) to verify the redox processes of  $\text{Cr}(\text{VI})$  and  $\text{Fe}(\text{II})$  on the hematite surface. Specifically, 0.5  $\text{g L}^{-1}$  of HNPs or HNRs were reacted with 20  $\mu\text{M}$   $\text{Fe}(\text{II})$  and  $\text{Cr}(\text{VI})$  at pH 3 and pH 7 for 180 minutes within a nitrogen-filled glovebox. The solids were then separated by filtration through 0.22  $\mu\text{m}$  filters, transferred to centrifuge tubes and sealed, and moved to a freeze-dryer outside the glovebox. After drying, the samples were purged with nitrogen, resealed, and rapidly transferred to the XPS chamber under high vacuum conditions. These steps minimized air exposure, thereby reducing, though not entirely preventing,  $\text{Fe}(\text{II})$  oxidation during the sample preparation and analysis.

### 2.3. Experimental procedure

The experiments were conducted within the nitrogen-filled glovebox, with an anaerobic atmosphere maintained by the continuous purging with  $\text{N}_2$  and circulation of the gas over a

copper catalyst. Typically, oxygen-free water, hematite suspension, NaCl solution,  $\text{Fe}(\text{II})$  stock solution and  $\text{Cr}(\text{VI})$  stock solutions were added into a 250 mL beaker, and the mixture was subjected to constant magnetic string at room temperature. The beakers were wrapped with tin foil to avoid any photochemical reactions that could affect the hematite.<sup>17,30</sup> The initial  $\text{Cr}(\text{VI})$  and  $\text{Fe}(\text{II})$  concentration was 20  $\mu\text{M}$ . The hematite concentration was 0.5  $\text{g L}^{-1}$ , and the ionic strength was controlled by 10 mM NaCl. The solution pH was adjusted to either  $3.0 \pm 0.1$  or  $5.0 \pm 0.1$  using 0.1 M NaOH and HCl solutions or maintained at  $7.0 \pm 0.1$  using PIPES buffer solution, a common practice in the literature to ensure pH stability.<sup>23</sup> At predetermined time intervals, samples were taken by filtration for subsequent analytical determinations. The influencing factors such as initial  $\text{Fe}(\text{II})$  concentrations (20 and 60  $\mu\text{M}$ ), initial hematite concentrations (0.5 and 2  $\text{g L}^{-1}$ ), and pH (3, 5 and 7) were investigated, respectively. Additionally, the adsorption of  $\text{Cr}(\text{VI})$  or  $\text{Fe}(\text{II})$  onto hematite, and the redox reaction between  $\text{Cr}(\text{VI})$  and  $\text{Fe}(\text{II})$  were also studied in binary systems. All experiments were performed at least twice to ensure the reproducibility of the results within 5%.

### 2.4. Analytical methods

At predetermined time intervals, aliquots of the hematite suspension were collected by filtration through a 0.22  $\mu\text{m}$  filter and the supernatant was then analyzed for the concentrations of  $\text{Cr}(\text{VI})$ , total Cr,  $\text{Fe}(\text{II})$ , and total Fe. Since  $\text{Cr}(\text{VI})$  and  $\text{Fe}(\text{II})$  in the supernatant after filtration still undergo ongoing reactions, prompt processing is essential for accurate determination of their concentrations (Text S2†). The concentration of  $\text{Cr}(\text{VI})$  was quantified by the 1,5-diphenylcarbonyldihydrazide method. Total Cr concentration was assessed using an inductively coupled plasma optical emission spectrometer (ICP-OES) (PerkinElmer Avio 200, USA). The concentration of  $\text{Cr}(\text{III})$  was inferred by subtracting the  $\text{Cr}(\text{VI})$  concentration from the total chromium concentration.  $\text{Fe}(\text{II})$  and total Fe concentrations in the supernatant were determined by the 1,10-phenanthroline method,<sup>31</sup> and the concentration of  $\text{Fe}(\text{III})$  was calculated by the difference between the total Fe and  $\text{Fe}(\text{II})$  concentrations.

## 3. Results and discussion

### 3.1. Structure and morphology of hematite nanocrystals

The structures and morphologies of the synthesized HNPs and HNRs were confirmed by XRD and TEM. The XRD pattern (Fig. S1†) revealed that both samples were composed of pure  $\alpha\text{-Fe}_2\text{O}_3$ , crystallizing in a rhombohedral hexagonal phase. TEM imaging Fig. 1 revealed that the morphology of HNPs and HNRs were well-defined hexagonal nanoplates and nanorods, aligning with previously reported results.<sup>4,14,17</sup> HNPs consist of two symmetrical hexagonal {001} facets and six equivalent {102} facets on the sides. The mean width and average thickness were measured to be 105.6 and 22.6 nm, respectively (Fig. 1a and b). High-resolution TEM (HRTEM) revealed a fringe of 0.25 nm, which corresponded to the

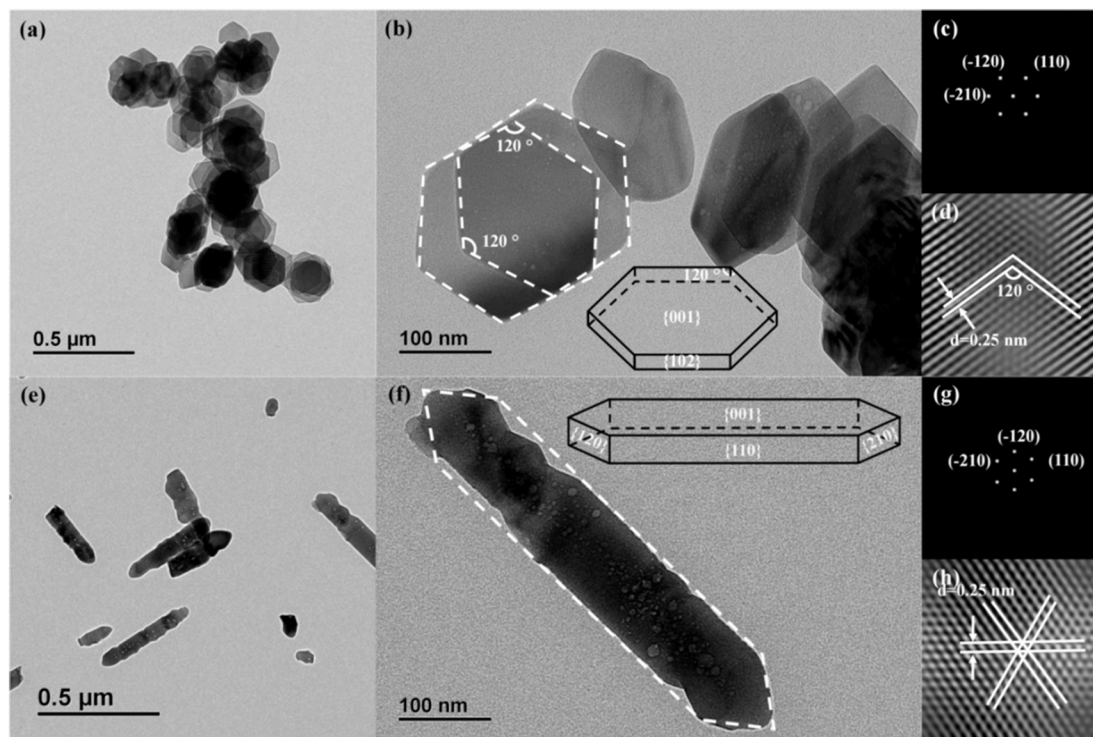


**Fig. 1** Representative morphology and crystalline structure of HNP and HNR. (a) TEM image, (b) a single nanoplatform, (c) FFT pattern, and (d) HRTEM image of HNP. (e) TEM image, (f) a single nanorod, (g) FFT pattern, and (h) HRTEM image of HNR. Insets in images (b) and (f) are schematic drawings of a nanoplatform and nanorod.

interplanar spacing of the  $\{-210\}$ ,  $\{-120\}$ , and  $\{110\}$  planes of HNP, as validated by the fast Fourier transform (FFT) pattern (Fig. 1c and d). For HNR, the mean dimensions were approximately 416.7 nm in length, and 88.9 nm in both width and height (Fig. 1e and f). The HRTEM images showed lattice fringes of 0.25 nm, consistent with the  $\{-210\}$ ,  $\{-120\}$ , and  $\{110\}$  planes of HNR, corroborated by the corresponding FFT patterns (Fig. 1g and h). Based on the above facet exposure analysis, HNP are predominantly composed of 80.18%  $\{001\}$  and 19.82%  $\{102\}$  facets (Fig. S2<sup>†</sup>), highlighting the dominance of the  $\{001\}$  facet exposure. In contrast, HNR are of about 39.15%  $\{001\}$ , 39.15%  $\{110\}$ , 10.85%  $\{120\}$ , and 10.85%  $\{210\}$  facets (Fig. S3<sup>†</sup>), suggesting a significant exposure of both  $\{001\}$  and  $\{110\}$  facet. The facile synthesis and precise control over the morphology and facet exposure of hematite are notably significant for revealing facet-dependent reactivity and optimizing performance. The B.E.T. specific surface areas were calculated to be  $10.875 \text{ m}^2 \text{ g}^{-1}$  for HNP and  $8.120 \text{ m}^2 \text{ g}^{-1}$  for HNR, respectively (Fig. S4<sup>†</sup>).

### 3.2. The facet-dependent Fe(II) or Cr(VI) adsorption on hematite

The adsorption of Fe(II) on HNP and HNR exhibited rapid kinetics, achieving equilibrium within 30 minutes (Fig. 2a). Higher pH favors Fe(II) adsorption, as typically encountered for cations adsorption onto iron minerals.<sup>32,33</sup>

The kinetic data were well-fitted with a pseudo-second-order model (Text S3<sup>†</sup> and Fig. 2b), indicating chemisorption mechanism. The adsorption kinetics constant for Fe(II) on HNR were found to be larger than that on HNP (Table S1<sup>†</sup>), indicating the faster adsorption of Fe(II) on HNR. The maximum adsorption capacities of Fe(II) on HNP ( $38.06 \mu\text{mol g}^{-1}$ ) was much higher than that of HNR ( $28.99 \mu\text{mol g}^{-1}$ ) at pH 7. Likewise, HNP exhibited a greater maximum adsorption capacity than HNR at pH 3 and pH 5 (Fig. 2a and Table S1<sup>†</sup>). The higher adsorption capacity of HNP is attributed to their larger specific surface area, which correlates positively with active adsorption site density. Surface area-normalized Fe(II) loadings for HNP were calculated as 0.19, 1.29 and  $2.11 \text{ \#Fe per nm}^2$  at pH 3, 5 and 7, respectively; for HNR, they were 0.20, 1.35 and  $2.15 \text{ \#Fe per nm}^2$  at the same pH values. Considering that HNP mainly expose  $\{001\}$  facets and HNR mainly expose  $\{001\}$  and  $\{110\}$  facets, the adsorption densities on these facets were estimated. At pH 3, the densities were  $0.24 \text{ \#Fe per nm}^2$  for  $\{001\}$  and  $0.27 \text{ \#Fe per nm}^2$  for  $\{110\}$  facets, at pH 5, they were  $1.61 \text{ \#Fe per nm}^2$  for  $\{001\}$  and  $1.82 \text{ \#Fe per nm}^2$  for  $\{110\}$  facets, and at pH 7, they were  $2.63 \text{ \#Fe per nm}^2$  for  $\{001\}$  and  $2.86 \text{ \#Fe per nm}^2$  for  $\{110\}$  facets, respectively. This suggests that the  $\{110\}$  facets of hematite have a marginally stronger binding affinity for Fe(II) than the  $\{001\}$  facets, as detailed in Table S2<sup>†</sup>. The facet-dependent Fe(II) binding to hematite surfaces reveals molecular-level reactivity of these surfaces, which is vital for elucidating the binding capacity

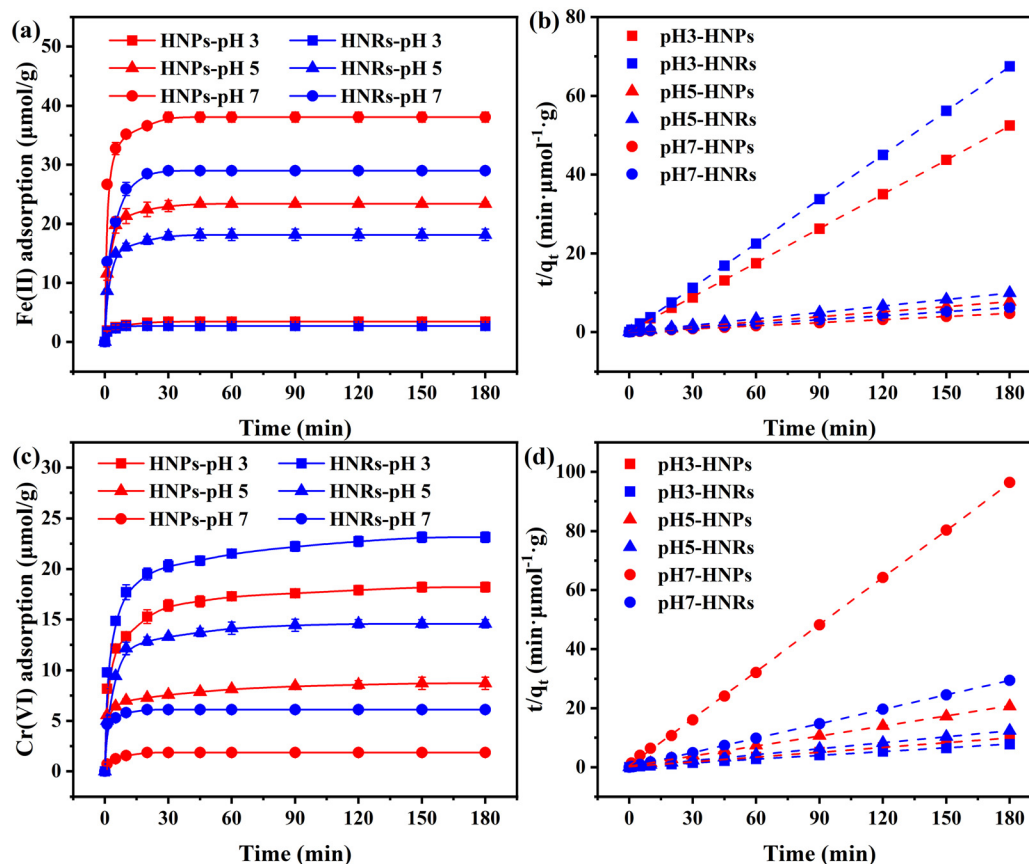


Fig. 2 Time dependent (a) Fe(II) and (c) Cr(VI) sorption by HNPs and HNRs. The pseudo-second-order kinetic model fittings for (b) Fe(II) and (d) Cr(VI). The initial concentration of Fe(II) and Cr(VI) was 20  $\mu\text{M}$ , the dosage of hematite was 0.5  $\text{g L}^{-1}$ , the ionic strength was 10 mM NaCl.

and the reducing properties of the Fe(II)–hematite system for pollutants.

The adsorption of Cr(VI) on HNPs and HNRs was rapid within 10 min and followed by a slow equilibrium stage (Fig. 2c). This initial rapid phase is likely due to the positively charged hematite surface. The point of zero charge ( $\text{pH}_{\text{pzc}}$ ) for HNPs and HNRs was determined to be pH 6.2 and pH 7.5, respectively (Fig. S5†). This positively charged surface at pH values below the  $\text{pH}_{\text{pzc}}$  enhances the adsorption of the anionic Cr(VI) due to electrostatic attractions. The adsorption of Cr(VI) increased with decreasing solution pH, consistent with previous studies where chromate adsorption tends to increase with decreasing pH below the zero-charge point of the mineral.<sup>4,34</sup>

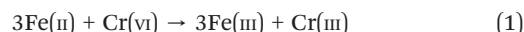
HNRs exhibited a significantly higher adsorption capacity for Cr(VI), outperforming HNPs by factors of 1.27, 1.67 and 3.27 at pH 3, pH 5 and pH 7, respectively (Table S2†). The adsorption kinetics conformed well to a pseudo-second-order model (Fig. 2d), indicative of a chemisorption process. Subsequent calculations of Cr(VI) adsorption on individual facets revealed densities of 1.26 and 3.13 #Cr per  $\text{nm}^2$  at pH 3, and 0.60 and 2.13 #Cr per  $\text{nm}^2$  at pH 5, and 0.13 and 1.03 #Cr per  $\text{nm}^2$  at pH 7, for the {001} and {110} facets, respectively. These results indicate a greater affinity for Cr(VI) binding onto the {110} facet of hematite, corroborating the

findings of Huang *et al.*,<sup>4</sup> which showed a higher adsorption of chromate species on the {110} facet compared to the {001} counterpart. This knowledge highlights the importance of facet engineering in hematite materials for the effective removal of Cr(VI).

### 3.3. Reduction of Cr(VI) by Fe(II)

The reductive conversion of Cr(VI) by Fe(II) was determined at initial concentrations of 20  $\mu\text{M}$  for both species under acidic and neutral conditions. As shown in Fig. 3, the Cr(VI) concentration decreased rapidly within 20 min, followed by a slow reduction phase.

The aqueous reduction of Cr(VI) by Fe(II) can be represented by the stoichiometric reaction:<sup>23–25</sup>



This indicates that three equivalents of Fe(II) are consumed per Cr(VI) reduced. The dashed line in Fig. 3, representing the concentration ratio of 3Fe(II), closely aligns with the reduction concentration ratio of Cr(VI) (solid line), confirming that Cr(VI) removal progresses stoichiometrically with Fe(II) depletion at 1:3 ratio.

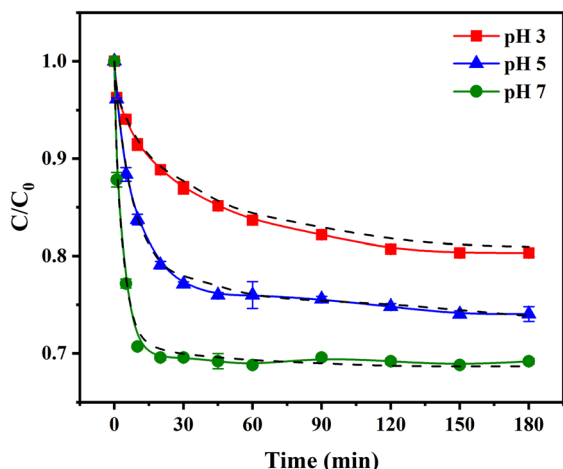


Fig. 3 Cr(VI) reduction kinetics by Fe(II) at different pH. The initial concentration of Cr(VI) and Fe(II) was 20  $\mu\text{M}$ , the ionic strength was 10 mM NaCl.

Additionally, the kinetics of the redox reaction is pH-dependent. The removal efficiency of Cr(VI) was around 20% at pH 3, 25% at pH 5, and 30% at pH 7. The Cr(VI) removal efficiency and kinetics were significantly higher at neutral pH (pH 7) than under acidic conditions (pH 3 and pH 5) (Text S4 and Fig. S6<sup>†</sup>), aligning with the findings of Buerge and Hug.<sup>23</sup> This result is attributed to the distinct speciation and reactivity of Fe(II) and Cr(VI) at different pH levels, along with the associated shifts in proton balance.<sup>23,26</sup>

### 3.4. Removal of Cr(VI) by hematite–Fe(II) couple

The anoxic removal performance of Cr(VI) by the prepared HNPs and HNRs coupled with Fe(II) was investigated under acidic (pH 3 and pH 5) and neutral (pH 7) conditions. Notably, at pH 3 and pH 5, the hematite–Fe(II) couple significantly outperformed the control treatments, which involved either Fe(II) or hematite alone (Fig. 4a and b). For example, at pH 3, the HNPs–Fe(II) system achieved a higher Cr(VI) removal rate of 76.59%, contrasting with 19.67% for Fe(II) alone (attributed to redox reactions) and 45.34% for HNPs alone (attributed to adsorption) at 180 min. This indicates there is a synergistic effect in Cr(VI) removal when both Fe(II) and hematite are present in the solution. The greater Cr(VI) removal achieved in the ternary system can be attributed to two primary factors: first, the presence of Fe(II) may enhance Cr(VI) adsorption onto hematite through increased electrostatic interactions. Second, the reducing property of Fe(II) is likely enhanced upon adsorption onto hematite compared to its aqueous state.<sup>27,28</sup> This could be due to the facilitation of electron transfer between the Fe(II) and the hematite surface, which in turn promotes the reduction of adsorbed Cr(VI) to Cr(III).

Interestingly, under neutral conditions (Fig. 4c and f), the removal efficiency of Cr(VI) in the hematite–Fe(II) system was slightly smaller than the sum of Cr(VI) removal efficiency when Fe(II) or hematite was used separately. It is noteworthy that at pH 7, hematite surfaces preferentially adsorbed Fe(II)

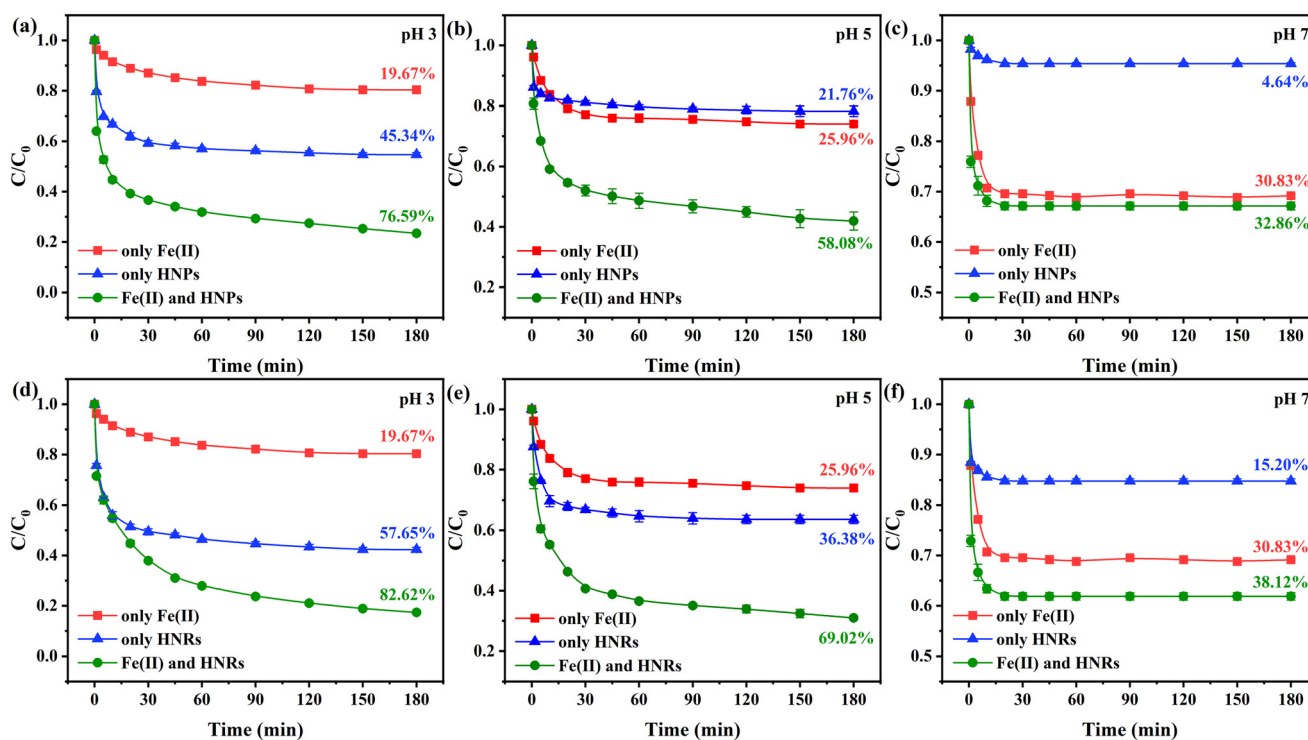


Fig. 4 Kinetics of Cr(VI) removal under (a and d) pH 3, (b and e) pH 5 and (c and f) pH 7 conditions with only Fe(II) or (a–c) HNPs or (d–f) HNRs and in the presence of both. The initial concentration of Fe(II) and Cr(VI) was 20  $\mu\text{M}$ , the dosage of hematite was 0.5 g L<sup>-1</sup>, the ionic strength was 10 mM NaCl.

over Cr(VI). Given that Fe(II) bound to hematite generally exhibits greater redox activity than free aqueous Fe(II),<sup>27,28</sup> we anticipated an enhanced Cr(VI) reduction in the hematite–Fe(II)–Cr(VI) ternary system compared to the Cr(VI)–Fe(II) binary system. However, the observed Cr(VI) removal efficiency in the ternary system was slightly lower than the combined individual efficiencies. This reduction in efficiency is likely due to the competitive adsorption of Fe(II), which limits the available adsorption sites for Cr(VI).

The evolution of Fe(II) in these systems (Fig. S7†) exhibited analogous outcomes, at pH 3, the Fe(II) removal efficiency surpassed the cumulative efficiency when Cr(VI) or HNPs was employed individually. This enhancement in Fe(II) removal is consistent with the observed increase in Cr(VI) removal in the ternary system as compared to the binary systems, suggesting a synergistic effect that boosts Fe(II) removal. However, under the same acidic conditions, the Fe(II) removal efficiency in the Fe(II)–Cr(VI)–HNPs ternary system was found to be lower than the sum of the efficiencies when Cr(VI) or HNPs were used separately. This difference could be due to the distinct mechanisms of Fe(II) removal in these systems. Given that Cr(VI) has a stronger adsorption affinity for HNPs than for HNPs, the formation of a Fe(II)–Cr(VI)–HNPs ternary complex is more pronounced, potentially favoring Fe(II) adsorption and thus limiting the redox reaction between Fe(II) and Cr(VI) in solution. Conversely, at pH 7, the Fe(II) removal efficiency in the ternary system was lower than the combined efficiency of Cr(VI) or hematite alone. This is attributed to the dominance of Fe(II) removal through reduction by Cr(VI) over Fe(II) removal *via* adsorption onto hematite. In the ternary system, competition between hematite and Cr(VI) for Fe(II) binding sites resulted in a decreased Fe(II) removal efficiency compared to the individual treatments with Cr(VI) or hematite. These results underscore the complexity of interfacial reactions. The total Fe concentration in the aqueous solution at pH 7 was much lower than at pH 3 (Fig. S8†), due to the enhanced adsorption of Fe(II) at higher pH values. Conversely, the removal of total Cr in solution at pH 7 (~30%) was significantly lower than that at pH 3 (~80%) (Fig. S8†), indicating that acidic pH conditions are more conducive to the retention of Cr in the solid phase.

Throughout the reaction, the ratio of Cr(VI) reduction to Fe(II) oxidation was observed to be higher than 1:3, indicating that Cr(VI) removal in solution involves both reduction and adsorption processes. Notably, Cr(VI) removal stagnated in the later stages of the reaction despite the presence of residual Fe(II) in solution (Fig. S8†). This phenomenon could be attributed to the formation of a passivation layer of Cr(III) on the hematite surface, which may hinder Fe(II) adsorption and impede electron transfer.<sup>35</sup> Since Fe(II) associated with iron oxides exhibits higher oxidation rate constants than aqueous Fe(II),<sup>36</sup> the reduction of Cr(VI) by Fe(II) is more efficient when Fe(II) is surface-bound. Therefore, the Cr(III) accumulation on the hematite surface likely reduced the amount of surface-bound Fe(II), leading to a decreased Cr(VI) removal rate in the later stages of the

reaction. Increasing the hematite dosage and Fe(II) concentration can mitigate this issue and improve Cr(VI) removal efficiency. For example, complete removal of Cr(VI) was achieved by increasing hematite dosage to 2.0 g L<sup>-1</sup> (Fig. S9†) or Fe(II) concentration to 60 μM (Fig. S10†).

The removal efficiency of Cr(VI) in HNPs–Fe(II) system was higher than that in HNPs–Fe(II) system at all pH conditions, with acidic conditions being more conducive to Cr(VI) removal. This result underscores the potential of HNPs–Fe(II) system for effective Cr(VI) removal in real-world environmental remediation scenarios. To elucidate the mechanism, the free corrosion potentials of HNPs and HNPs were measured in the presence of 20 μM Fe(II) and Cr(VI) using Tafel polarization diagrams. HNPs exhibited a greater propensity to donate electrons, as indicated by their more negative free corrosion potential (−0.062 V) compared to HNPs (−0.004 V) (Fig. 5). Since an electrode with a more negative free corrosion potential facilitates a higher electron transfer rate,<sup>37,38</sup> the superior electron transport capability of HNPs underpins the more effective Cr(VI) removal when coupled with Fe(II) compared to HNPs.

### 3.5. Possible mechanisms of the facet-dependent Cr(VI) removal in the presence of Fe(II)

XPS was utilized to determine the valence states of Cr and Fe on the hematite surface in order to reveal the detailed mechanism of Cr(VI) removal. The XPS spectra demonstrated the coexistence of Cr, Fe, and O on the hematite surface (Fig. S11†). As shown in Fig. 6, peaks located at 588.9 eV and 585.8 eV in the Cr 2p<sub>1/2</sub> region correspond to Cr(VI) and Cr(III), respectively, while peaks at 578.3 eV and 575.7 eV in the Cr 2p<sub>3/2</sub> region are indicative of Cr(VI) and Cr(III), respectively.<sup>39,40</sup> Semi-quantification of Cr species on the surface of hematite revealed that Cr(III) predominated, constituting approximately 70%, with Cr(VI) at about 30%. Correspondingly, the surface Fe species analysis revealed a higher proportion of Fe(III) compared to Fe(II) under both pH

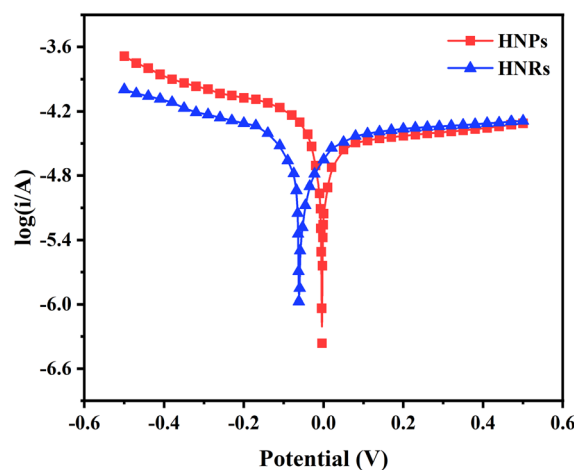


Fig. 5 Tafel scans in the presence of 20 μM Fe(II) and Cr(VI).

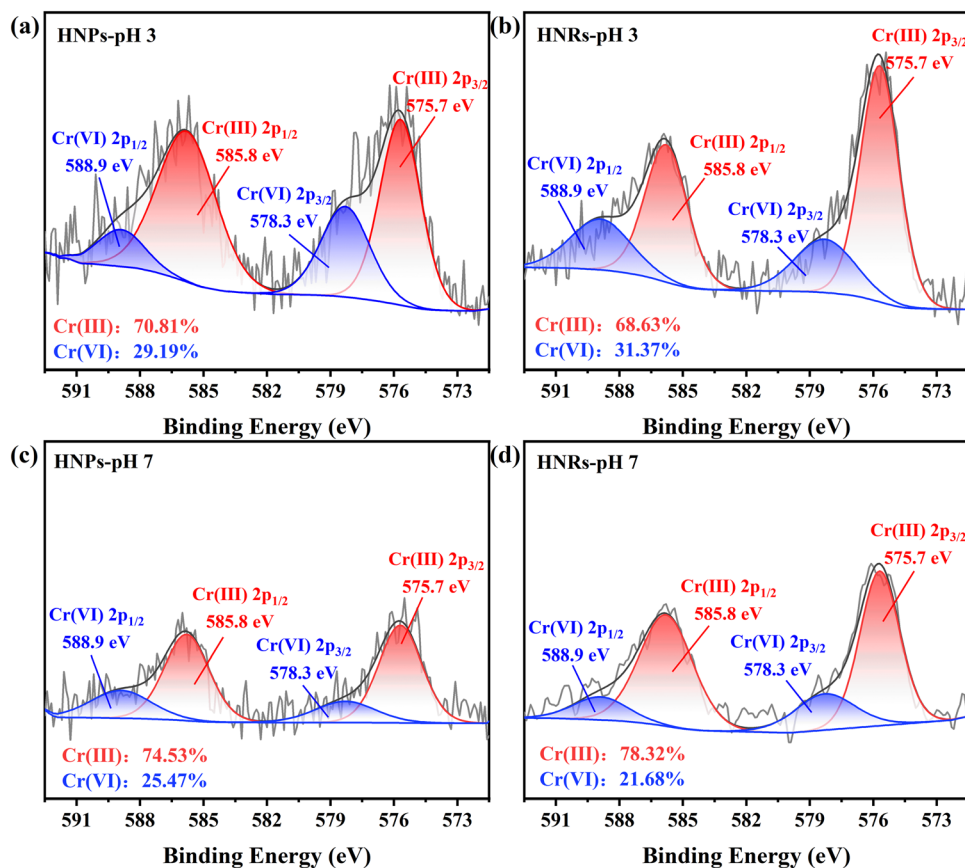


Fig. 6 Cr 2p XPS spectra of the reacted (a and c) HNPs and (b and d) HNRs with 20  $\mu\text{M}$  Fe(II) and Cr(VI) under (a and b) pH 3 and (c and d) pH 7 for 180 min.

conditions (Fig. S12<sup>†</sup>). This indicates that the hematite–Fe(II) system effectively facilitates the adsorption and reduction of Cr(VI).

The final distribution of initially introduced Cr(VI) was ascertained by measuring total chromium and Cr(VI) in the aqueous phase (Fig. S8a–d<sup>†</sup>) and correlating this with the solid-phase percentages of Cr(III) and Cr(VI), as depicted in Fig. 7. HNRs–Fe(II) demonstrated superior Cr(VI) removal efficiency, with a greater proportion of chromium being immobilized on the solid surface under acidic conditions compared to neutral conditions. At pH 3, the adsorption of Cr(VI) onto the hematite surface is more pronounced than its reduction by Fe(II) in the aqueous solution. The adsorption of Cr(VI) imparts a more negative charge to the hematite surface, which in turn enhances the adsorption of the cationic Fe(II) and Cr(III). The bound Fe(II) can then reduce the adsorbed Cr(VI) to Cr(III) on the hematite surface. Consequently, the majority of Cr(VI) was reduced to Cr(III) and all the Cr(III) was retained in the solid phase. Conversely, at pH 7, over 60% of the initial Cr(VI) remained in solution, with aqueous Cr(III) constituting approximately 20%. This is attributed to the preferential adsorption of Fe(II) onto hematite, which makes the hematite surface more positive and is less favorable for the adsorption of Cr(III), leading to a lower removal efficiency under neutral conditions.

The interactions between aqueous Fe(II) and iron oxides are intricate, encompassing adsorption, electron transfer, conduction, atom exchange, and reductive dissolution.<sup>21,41,42</sup> Consequently, in the Fe(II)–hematite system, the electron

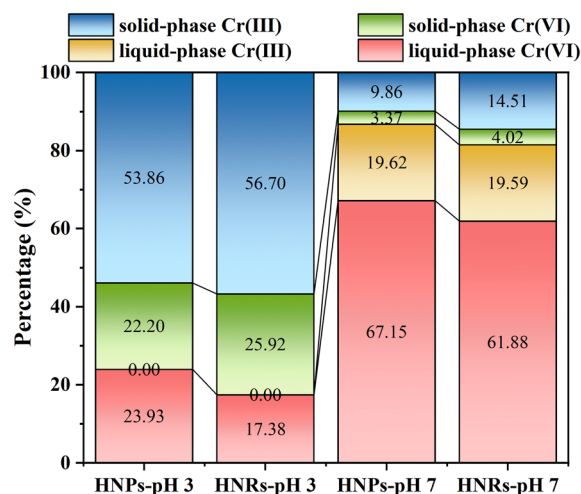


Fig. 7 Proportions of various Cr at the end of reaction in various reaction systems involving hematite, Cr(VI), and Fe(II). The initial concentration of Cr(VI) and Fe(II) was 20  $\mu\text{M}$ , the dosage of hematite was 0.5  $\text{g L}^{-1}$ , the ionic strength was 10 mM NaCl.

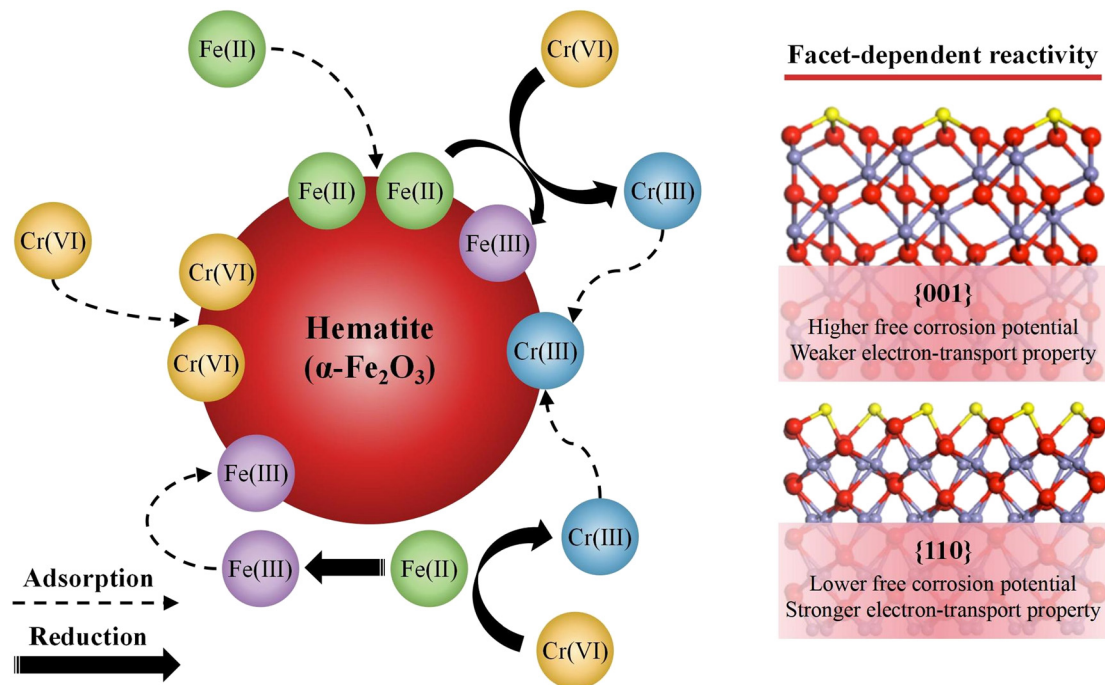


Fig. 8 The schematic diagram of the underlying mechanism of facet-dependent Cr(vi) removal by hematite coupled Fe(ii).

transfer mechanism involved in Cr(vi) reduction is notably complex. Based on the above analysis, a plausible mechanism for Cr(vi) removal by hematite coupled with Fe(ii) is depicted in Fig. 8. This mechanism encompasses concurrent stages: the adsorption of Cr(vi) and Fe(ii) onto hematite nanoparticles, reduction of Cr(vi) to Cr(iii) by aqueous Fe(ii) and bound Fe(ii), adsorption of Cr(iii) and Fe(iii) onto hematite surface. The adsorption of both Cr(vi) and Fe(ii) on the hematite surface is influenced by the crystal facets, with the {110} facets showing a higher affinity for these species. Moreover, the {110} facets exhibit a lower free corrosion potential, which correlates with enhanced electron transport capabilities, thereby contributing to a stronger reducibility.

## 4. Conclusion

This study demonstrated the facet-dependent activity of hematite–Fe(ii) couple for Cr(vi) removal. The synthesized hematite nanoplate (HNPs) predominantly composed of {001} facets, while nanorod (HNRs) displayed significant exposure of both {001} and {110} facets. The adsorption of Fe(ii) and Cr(vi) on hematite surfaces was highly sensitive to both the crystal facets and pH. Specifically, the {110} facets exhibited greater adsorption capacity for both Fe(ii) and Cr(vi) than the {001} facets. Additionally, Fe(ii) adsorption was favored at higher pH values, while Cr(vi) adsorption was more pronounced at lower pH values. The stoichiometric redox reaction between Fe(ii) and Cr(vi) was confirmed, and the removal efficiency and kinetics of Cr(vi) by Fe(ii) were significantly higher at neutral pH compared to acidic conditions. The hematite–Fe(ii) couple demonstrated a synergistic effect in Cr(vi) removal under acidic conditions, with

a higher proportion of chromium being immobilized on the solid surface compared to neutral conditions. This enhanced Cr(vi) removal in the ternary system is attributed to the increased Cr(vi) adsorption onto hematite and the accelerated Cr(vi) reduction by Fe(ii) bound to hematite. Conversely, at neutral pH, the Cr(vi) removal efficiency in the ternary system was slightly lower than the combined individual efficiencies, likely due to the competitive adsorption of Fe(ii), which limits Cr(vi) adsorption. HNRs–Fe(ii) displayed greater Cr(vi) removal efficiency compared to HNPs–Fe(ii). This superiority is attributed to the lower free corrosion potential and enhanced electron transport capabilities of HNRs. These findings deepen our understanding of the interactions between naturally occurring Fe(ii) and hematite in reducing and immobilizing Cr(vi), indicating a possible natural attenuation mechanism for Cr(vi) in soils. Furthermore, they underscore the importance of hematite nanocrystals in the remediation of Cr(vi)-contaminated environments and highlight the potential of facet engineering in enhancing remediation efficiency.

## Data availability

The data supporting this article have been included as part of the main article and ESI.†

## Author contributions

Shengnan Zhang: conceptualization, writing – original draft, methodology and investigation. Lingyi Li and Junxue Li: validation, data curation and formal analysis. Wei Cheng:

writing – review & editing, funding acquisition, project administration.

## Conflicts of interest

The authors declare that they have no known competing financial interests or personal relationships that could have appeared to influence the work reported in this paper.

## Acknowledgements

This work was supported by the Natural Science Foundations of China (No. NSFC22006165).

## References

- 1 L. Ma, N. Chen, C. Feng and Q. Yang, Recent Advances in Enhanced Technology of Cr(VI) Bioreduction in Aqueous Condition: A Review, *Chemosphere*, 2024, **351**, 141176.
- 2 E. C. Rada, M. Schiavon and V. Torretta, A Regulatory Strategy for the Emission Control of Hexavalent Chromium from Waste-to-Energy Plants, *J. Cleaner Prod.*, 2021, **278**, 123415.
- 3 T. Huang, L. Zhou, Z. Cao, S. Zhang and L. Liu, A Microwave Irradiation-Persulfate-Formate System for Achieving the Detoxification and Alkali-Activated Composite Geopolymerization of the Chromate-Contaminated Soil, *Ecotoxicol. Environ. Saf.*, 2021, **217**, 112233.
- 4 X. Huang, X. Hou, F. Song, J. Zhao and L. Zhang, Facet-Dependent Cr(VI) Adsorption of Hematite Nanocrystals, *Environ. Sci. Technol.*, 2016, **50**, 1964–1972.
- 5 S. Jiang, X. Yan, C. L. Peacock, S. Zhang, W. Li, J. Zhang, X. Feng, F. Liu and H. Yin, Adsorption of Cr(VI) on Al-Substituted Hematites and Its Reduction and Retention in the Presence of Fe<sup>2+</sup> under Conditions Similar to Subsurface Soil Environments, *J. Hazard. Mater.*, 2020, **390**, 122014.
- 6 Z. Yang, Y. Li, X. Wang, J. Li, J. Wang and G. Zhang, Facet-Dependent Activation of Oxalic Acid over Hematite Nanocrystals under the Irradiation of Visible Light for Efficient Degradation of Pollutants, *J. Environ. Sci.*, 2024, **142**, 204–214.
- 7 X. Jin, D. Wu, C. Liu, S. Huang, Z. Zhou, H. Wu, X. Chen, M. Huang, S. Zhou and C. Gu, Facet Effect of Hematite on the Hydrolysis of Phthalate Esters under Ambient Humidity Conditions, *Nat. Commun.*, 2022, **13**, 6125.
- 8 X. Zhou, Q. Xu, W. Lei, T. Zhang, X. Qi, G. Liu, K. Deng and J. Yu, Origin of Tunable Photocatalytic Selectivity of Well-Defined  $\alpha$ -Fe<sub>2</sub>O<sub>3</sub> Nanocrystals, *Small*, 2014, **10**, 674–679.
- 9 S. Chatman, P. Zarzycki and K. M. Rosso, Surface Potentials of (001), (012), (113) Hematite ( $\alpha$ -Fe<sub>2</sub>O<sub>3</sub>) Crystal Faces in Aqueous Solution, *Phys. Chem. Chem. Phys.*, 2013, **15**, 13911.
- 10 S. Bandi and A. K. Srivastav, Understanding the Growth Mechanism of Hematite Nanoparticles: The Role of Maghemite as an Intermediate Phase, *Cryst. Growth Des.*, 2021, **21**, 16–22.
- 11 L. Yan, T. Chan and C. Jing, Arsenic Adsorption on Hematite Facets: Spectroscopy and DFT Study, *Environ. Sci.:Nano*, 2020, **7**, 3927–3939.
- 12 R. M. Bolanz, M. Wierzbicka-Wieczorek, M. Čaplovičová, P. Uhlík, J. Göttlicher, R. Steininger and J. Majzlan, Structural Incorporation of As<sup>5+</sup> into Hematite, *Environ. Sci. Technol.*, 2013, **47**, 9140–9147.
- 13 A. W. Lounsbury, R. Wang, D. L. Plata, N. Billmyer, C. Muhich, K. Kanie, T. Sugimoto, D. Peak and J. B. Zimmerman, Preferential Adsorption of Selenium Oxyanions onto {110} and {012} Nano-Hematite Facets, *J. Colloid Interface Sci.*, 2019, **537**, 465–474.
- 14 Z. Shen, Z. Zhang, T. Li, Q. Yao, T. Zhang and W. Chen, Facet-Dependent Adsorption and Fractionation of Natural Organic Matter on Crystalline Metal Oxide Nanoparticles, *Environ. Sci. Technol.*, 2020, **54**, 8622–8631.
- 15 X. Zhou, J. Lan, G. Liu, K. Deng, Y. Yang, G. Nie, J. Yu and L. Zhi, Facet-Mediated Photodegradation of Organic Dye over Hematite Architectures by Visible Light, *Angew. Chem., Int. Ed.*, 2012, **51**, 178–182.
- 16 K. Sivula, F. Le Formal and M. Grätzel, Solar Water Splitting: Progress Using Hematite ( $\alpha$ -Fe<sub>2</sub>O<sub>3</sub>) Photoelectrodes, *ChemSusChem*, 2011, **4**, 432–449.
- 17 T. Hao, Y. Huang, F. Li, Y. Wu and L. Fang, Facet-Dependent Fe(II) Redox Chemistry on Iron Oxide for Organic Pollutant Transformation and Mechanisms, *Water Res.*, 2022, **219**, 118587.
- 18 F. Wu, J. Hua, J. Zhou, Y. Liu, S. Long, Y. Fei and C. Liu, Facet-Specific Reactivity of Hematite Nanocrystals during Fe(II)-Catalyzed Recrystallization, *Chem. Geol.*, 2021, **583**, 120460.
- 19 R. Han, J. Lv, S. Zhang and S. Zhang, Hematite Facet-Mediated Microbial Dissimilatory Iron Reduction and Production of Reactive Oxygen Species during Aerobic Oxidation, *Water Res.*, 2021, **195**, 116988.
- 20 X. Huang, X. Hou, X. Zhang, K. M. Rosso and L. Zhang, Facet-Dependent Contaminant Removal Properties of Hematite Nanocrystals and Their Environmental Implications, *Environ. Sci.:Nano*, 2018, **5**, 1790–1806.
- 21 X. Huang, X. Hou, J. Zhao and L. Zhang, Hematite Facet Confined Ferrous Ions as High Efficient Fenton Catalysts to Degrade Organic Contaminants by Lowering H<sub>2</sub>O<sub>2</sub> Decomposition Energetic Span, *Appl. Catal., B*, 2016, **181**, 127–137.
- 22 L. Fang, B. Gao, F. Li, K. Liu and J. Chi, The Nature of Metal Atoms Incorporated in Hematite Determines Oxygen Activation by Surface-Bound Fe(II) for As(III) Oxidation, *Water Res.*, 2022, **227**, 119351.
- 23 I. J. Buerge and S. J. Hug, Kinetics and pH Dependence of Chromium(VI) Reduction by Iron(II), *Environ. Sci. Technol.*, 1997, **31**, 1426–1432.
- 24 M. Pettine, L. D'Ottone, L. Campanella, F. J. Millero and R. Passino, The Reduction of Chromium (VI) by Iron (II) in Aqueous Solutions, *Geochim. Cosmochim. Acta*, 1998, **62**, 1509–1519.
- 25 Q. A. Nguyen, B. Kim, H. Y. Chung, A. Q. K. Nguyen, J. Kim and K. Kim, Reductive Transformation of Hexavalent Chromium by Ferrous Ions in a Frozen Environment: Mechanism, Kinetics, and Environmental Implications, *Ecotoxicol. Environ. Saf.*, 2021, **208**, 111735.

- 26 J. H. Espenson, Rate Studies on the Primary Step of the Reduction of Chromium(VI) by Iron(II), *J. Am. Chem. Soc.*, 1970, **92**, 1880–1883.
- 27 E. Silvester, L. Charlet, C. Tournassat, A. Géhin, J.-M. Grenèche and E. Liger, Redox Potential Measurements and Mössbauer Spectrometry of Fe<sup>II</sup> Adsorbed onto Fe<sup>III</sup> (Oxyhydr)Oxides, *Geochim. Cosmochim. Acta*, 2005, **69**, 4801–4815.
- 28 W. Stumm and B. Sulzberger, The Cycling of Iron in Natural Environments: Considerations Based on Laboratory Studies of Heterogeneous Redox Processes, *Geochim. Cosmochim. Acta*, 1992, **56**, 3233–3257.
- 29 J. Lv, Y. Miao, Z. Huang, R. Han and S. Zhang, Facet-Mediated Adsorption and Molecular Fractionation of Humic Substances on Hematite Surfaces, *Environ. Sci. Technol.*, 2018, **52**, 11660.
- 30 A. K. Patra, S. K. Kundu, A. Bhaumik and D. Kim, Morphology Evolution of Single-Crystalline Hematite Nanocrystals: Magnetically Recoverable Nanocatalysts for Enhanced Facet-Driven Photoredox Activity, *Nanoscale*, 2016, **8**, 365–377.
- 31 A. E. Harvey, J. A. Smart and E. S. Amis, Simultaneous Spectrophotometric Determination of Iron(II) and Total Iron with 1,10-Phenanthroline, *Anal. Chem.*, 1955, **27**, 26–29.
- 32 S. M. Nomaan, S. N. Stokes, J. Han and L. E. Katz, Application of Spectroscopic Evidence to Diffuse Layer Model (DLM) Parameter Estimation for Cation Adsorption onto Ferrihydrite in Single- and Bi-Solute Systems, *Chem. Geol.*, 2021, **573**, 120199.
- 33 W. Cheng, J. Li, J. Sun, T. Luo, R. Marsac, J.-F. Boily and K. Hanna, Nalidixic Acid and Fe(II)/Cu(II) Coadsorption at Goethite and Akaganéite Surfaces, *Environ. Sci. Technol.*, 2023, **57**, 15680–15692.
- 34 K. Mesuere and W. Fish, Chromate and Oxalate Adsorption on Goethite. 2. Surface Complexation Modeling of Competitive Adsorption, *Environ. Sci. Technol.*, 1992, **26**, 2365–2370.
- 35 M. E. Bishop, H. Dong, P. Glasser, B. R. Briggs, M. Pentrak, J. W. Stucki, M. I. Boyanov, K. M. Kemner and L. Kovarik, Reactivity of Redox Cycled Fe-Bearing Subsurface Sediments towards Hexavalent Chromium Reduction, *Geochim. Cosmochim. Acta*, 2019, **252**, 88–106.
- 36 C. A. Gorski, R. Edwards, M. Sander, T. B. Hofstetter and S. M. Stewart, Thermodynamic Characterization of Iron Oxide-Aqueous Fe<sup>2+</sup> Redox Couples, *Environ. Sci. Technol.*, 2016, **50**, 8538–8547.
- 37 W. Shen, Y. Mu, T. Xiao and Z. Ai, Magnetic Fe<sub>3</sub>O<sub>4</sub>-FeB Nanocomposites with Promoted Cr(VI) Removal Performance, *Chem. Eng. J.*, 2016, **285**, 57–68.
- 38 Y. Mu, Z. Ai, L. Zhang and F. Song, Insight into Core-Shell Dependent Anoxic Cr(VI) Removal with Fe@Fe<sub>2</sub>O<sub>3</sub> Nanowires: Indispensable Role of Surface Bound Fe(II), *ACS Appl. Mater. Interfaces*, 2015, **7**, 1997–2005.
- 39 M. C. Biesinger, C. Brown, J. R. Mycroft, R. D. Davidson and N. S. McIntyre, X-ray Photoelectron Spectroscopy Studies of Chromium Compounds, *Surf. Interface Anal.*, 2004, **225**, 86–92.
- 40 M. C. Biesinger, B. P. Payne, A. P. Grosvenor, L. W. M. Lau, A. R. Gerson, R. St and C. Smart, Resolving Surface Chemical States in XPS Analysis of First Row Transition Metals, Oxides and Hydroxides: Cr, Mn, Fe, Co and Ni, *Appl. Surf. Sci.*, 2011, **257**, 2717–2730.
- 41 J. G. Catalano, P. Fenter, C. Park, Z. Zhang and K. M. Rosso, Structure and Oxidation State of Hematite Surfaces Reacted with Aqueous Fe(II) at Acidic and Neutral pH, *Geochim. Cosmochim. Acta*, 2010, **74**, 1498–1512.
- 42 R. M. Handler, B. L. Beard, C. M. Johnson and M. M. Scherer, Atom Exchange between Aqueous Fe(II) and Goethite: An Fe Isotope Tracer Study, *Environ. Sci. Technol.*, 2009, **43**, 1102–1107.